photonics

Article

Low-Cost High-Speed Fiber-Coupled Interferometer for Precise Surface Profilometry

Sebastian Hagemeier *, Yijian Zou, Tobias Pahl, Felix Rosenthal and Peter Lehmann

Measurement Technology Group, Faculty of Electrical Engineering and Computer Science, University of Kassel, Wilhelmshoeher Allee 71, 34121 Kassel, Germany; yijian.zou@uni-kassel.de (Y.Z.); tobias.pahl@uni-kassel.de (T.P.); f.rosenthal@uni-kassel.de (F.R.); p.lehmann@uni-kassel.de (P.L.)
* Correspondence: s.hagemeier@uni-kassel.de

Abstract: Due to their contactless and fast measuring capabilities, laser interferometers represent an interesting alternative to tactile stylus instruments for surface profilometry. In addition to these outstanding attributes, acquisition costs play a major role in industry, limiting the frequent use of optical profilometers, which are significantly more expensive than tactile profilometers. We present a low-cost laser distance-measuring interferometer featuring axial repeatability below 1 nm at acquisition rates of 38,000 height values per second. The sensor's performance is validated on several surface standards, achieving lateral scan velocities up to 160 mm/s. Further to high scan velocities, the high acquisition rate enables improved measurement accuracy by averaging measured height values. For example, the standard deviation of 625 pm for repeated measurements can be reduced to 265 pm at the expense of the data rate. However, the sensor concept provides the potential for further improvements in data rate and measurement repeatability.

Keywords: profilometer; fiber sensor; high-speed measurement; low-cost laser interferometer; additive manufacturing

Citation: Hagemeier, S.; Zou, Y.; Pahl, T.; Rosenthal, F.; Lehmann, P. Low-Cost High-Speed Fiber-Coupled Interferometer for Precise Surface Profilometry. *Photonics* **2024**, *11*, 674. https://doi.org/10.3390/photonics11070674

Received: 13 June 2024
Revised: 16 July 2024
Accepted: 17 July 2024
Published: 19 July 2024

1. Introduction

Surface profilometry is widely applied in different branches of industry in order to ensure the quality of manufactured products. For this purpose, tactile stylus instruments, where the tip of the instrument is in touch with the surface under investigation while either the tip or the measurement object is laterally moved, are most widely used. The measured surface height results from the axial deflection of the probe tip [1–4]. However, these instruments suffer from low lateral scan velocities, usually below 1 mm/s, and possible surface damage provoked by mechanical contact with the stylus tip. Due to their contactless measuring capabilities and faster lateral scan velocities, optical instruments represent an alternative to surface profilometry. An example of an optical point-wise measuring instrument is the chromatic confocal sensor, where the depth discrimination originates from wavelength-dependent refraction [5,6]. In addition to special optical components such as diffractive optical elements, a spectrometer is needed to obtain height values. This limits the maximum data rate and increases the manufacturing costs of such sensors. Further, microscope objectives are commonly used, resulting in relatively large dimensions of the sensor probe head compared to other point-wise measuring systems. With this type of sensor, detection rates of up to 70 kHz with an axial resolution of 40 nm can be achieved, as Wertjanz et al. [7] reported. The laser focus sensor presented by Mastylo et al. [8] uses a hologram laser unit adopted from CD/DVD player technology as the main component. This reduces the acquisition and adjustment costs. However, the lateral scan velocity of the presented sensor is limited to 6 mm/s.

Other sensors are based on interferometric measuring principles, which provide improved axial accuracy. One example is the point-wise measuring coherence scanning interferometer, as presented in several studies [9–11]. The advantage of this sensor is high axial accuracy due to phase evaluation and an unambiguous determination by combining phase measurements with fringe order determination based on the maximum position of the signal envelope. Furthermore, since a tilted reference mirror is used for depth discrimination, no mechanical scan is necessary. However, a line scan camera is needed, which leads to a limited rate of height values due to the limited camera frame rate and an increase in the sensor costs. Moreover, this sensor approach suffers from optical dispersion and a signal contrast limited by the dynamic range of the camera as a consequence of the intensity offset. A common-path laser interferometer is presented in [12], where the optical path length difference (OPD) is modulated by an oscillating bending beam. Due to the simple arrangement and commercially available components, both acquisition and assembly costs are low. However, the mass inertia of the bending beam in combination with the probe head results in a typical oscillation frequency of 1 kHz and, thus, limits the acquisition rate. A similar approach is shown in [13,14], where the modulation of the OPD is performed by stretching a fiber or using an electro-optical modulator, leading to a maximum oscillation frequency of 5 kHz. Another laser interferometer uses an ultrasonic transducer as reference mirror to modulate the OPD with an oscillation frequency of 58 kHz, leading to a maximum acquisition rate of 116 kHz, as reported in [15]. A more compact sensor design is presented in [16,17], where reduced geometrical dimensions come at the expense of a reduced oscillation frequency of 40 kHz.

In this contribution, we introduce a fiber interferometric confocal distance sensor (FICDS) for surface profilometry, on the basis of a modulated OPD as presented in [17]. However, in this setup, we use a fiber coupler instead of a beam splitter for separating measurement and reference arm and, thus, simplify the sensor assembly. Furthermore, the sensor housing and guiding grooves for the optical components are fabricated using an additive manufacturing method. This approach reduces the effort that is needed for the assembly and adjustment of the sensor head. Since a reference mirror oscillating at 38 kHz is used in this arrangement, a maximum data rate of 76 kHz can be achieved. The sensor configuration and signal processing are introduced in the following sections. Finally, the sensor is characterized by several measurements performed on specimens of different surface texture. Surface profiles are scanned at high lateral scan velocities up to 160 mm/s. Besides profilometry, multiple fields of application exist for this sensor approach. For example, the sensor can be used to measure the axial and lateral run-out of a rotational table, as reported by Riebeling et al. [18]. Another application in combination with 3D-microscopes is to record and correct for vibration influences, as demonstrated in [19]. Further, this type of sensor can be used to measure the fast-changing layer thickness of evaporating fluid layers [16], for example.

2. Sensor Setup

The sensor setup and signal analysis are discussed in this section. An overview of the interferometric sensor head (and the accompanying electronics and data processing modules) is given in Figure 1. As part of the DAC/ADC high-speed mezzanine card (HMSC) from Altera Cooperation [20], the digital-to-analog converter (DAC) generates a sinusoidal voltage signal, which is amplified by an actor driver (AD) circuit and used to deflect the piezoelectric actuator (A) located in the sensor head. The actuator is part of the interferometric setup located in the sensor head, as discussed in more detail in Section 2.1. For an optical connection to the interferometer, two FC/APC fiber connectors are mounted on the sensor housing in order to couple laser light, emitted by a fiber-coupled distributed feedback laser with a linewidth <2 MHz [21] and controlled by the laser driver (LD), into the sensor head and to guide the interference signals to a photodiode. The interference signal is then converted into an electric signal and amplified by a transimpedance amplifier as part of the photodiode driver (PD). The resulting signal is then preprocessed by the signal processing unit (SPU) and digitized by the analog-to-digital converter (ADC) of the HSMC. Finally, the height values are calculated from the digitized signals in real time by a field programmable gate array (FPGA) Cyclone V as part of a SoCKit development board [22] from terasIC Inc. (Hsinchu in Taiwan). The resulting height values are transferred to the PC. All electronic components are explained in detail in [16].

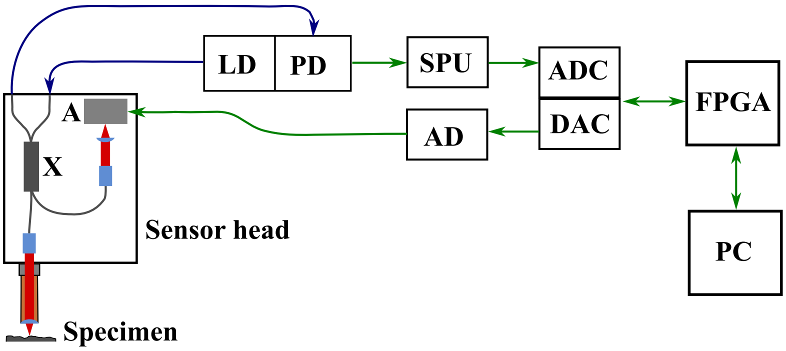

Figure 1. Overview of the sensor head and the surrounding electronic components. The green lines represent electric connections, whereas the blue and red lines indicate fiber and free-beam optical connections. X = x-coupler, A = actuator (ultrasonic transducer), LD = laser driver, PD = photodiode driver, SPU = signal processing unit, AD = actor driver, ADC = analog-to-digital converter, DAC = digital-to-analog converter, FPGA = field programmable gate array, and PC = personal computer.

2.1. Interferometric Sensor

In previous sensor designs, the measurement and reference arms are separated by use of a beam splitter cube, as reported in [15,17]. This increases the assembly and adjustment time of the optical sensor components, especially if long-distance reference or measurement arms are required. In order to minimize these efforts, the splitting into measurement and reference arm is performed by a fiber x-coupler in the FICDS, as presented in Figure 2a,b. Both the measurement and the reference beams are collimated by a GRIN lens located at the end-face of the corresponding fiber ferrule. The connecting end faces between the GRIN lenses and fiber ferrules exhibit an eight-degree angle to avoid spurious reflections and, thus, are connected in contact with each other. The GRIN lens used is a rod lens from Grintech GmbH (Jena in Germany) [23] with a pitch of 0.25. Fiber ferrules and GRIN lenses have the same outer diameter and are aligned with respect to each other using a glass sleeve to ensure that the optical path is not displaced. After collimation, the two beams are focused on the polished surface of an ultrasonic transducer, which acts as a reference mirror, and the surface of the specimen by aspherical focusing lenses. These lenses are characterized by an outer diameter of 2.4 mm, a numerical aperture (NA) of 0.58, and a working distance of 0.8 mm. The light reflected at the reference mirror and the surface of the specimen is collected by the focusing lenses and again coupled into the fibers of the coupler, where the two beams superpose. Then, the resulting interference signal is transferred to the photodiode and processed as previously described in Figure 1.

In contrast to common-path interferometers [12,13,24] or other setups [25], where vibrations to the optical fiber affect the measurement and reference arm in the same way, any motion of the fiber-based measurement or reference arm leads to different phase shifts of the laser beams guided by the single-mode fibers in the presented sensor setup. This directly changes the phase difference between measurement and reference beams. Consequently, the additional phase difference results in a corresponding height measurement error and, thus, increases the measurement uncertainty, as reported in [16]. To avoid these measurement deviations, the x-coupler and all its optical fibers are encapsulated in wax within the sensor housing. Note that the whole sensor housing, including all the mounts of the optical components, has been additively manufactured using the stereo-lithography 3D-printer Photon Mono M5s from Anycubic Ltd. (Hongkong in China) [26]. However, the sensor probe tip in the measurement arm is made from metal using a milling machine, but can also be additively manufactured like the rest of the sensor housing. For comparison, a free-beam interferometer manufactured from metal by a milling machine is depicted in Figure 2c. In this setup, the incoming laser beam is split into measurement and reference arms by a beam-splitter cube. In addition, a right-angle prism mirror is placed in the reference arm to reduce the geometric dimensions of the sensor. Electronic circuits, GRIN, and focusing lenses are identical to those used in the sensor setup of the FICDS. Compared to the FICDS, the production and the alignment effort of the free-beam interferometer are significantly higher. In both setups, the probe tip has a small outer diameter of approximately 3.5 mm at the lower end. The collimated laser beam entering the probe tip is focused by an aspherical lens mounted at the end face of each probe tip. Note that an exemplary geometry of the probe tip is shown here, which can be adapted to the corresponding application scenario. For example, for the measurement of drill hole walls, a prism is attached to the end face of the sensor tip to deflect the laser beam by an angle of 90 degrees, similar to the solution presented in [12,27].

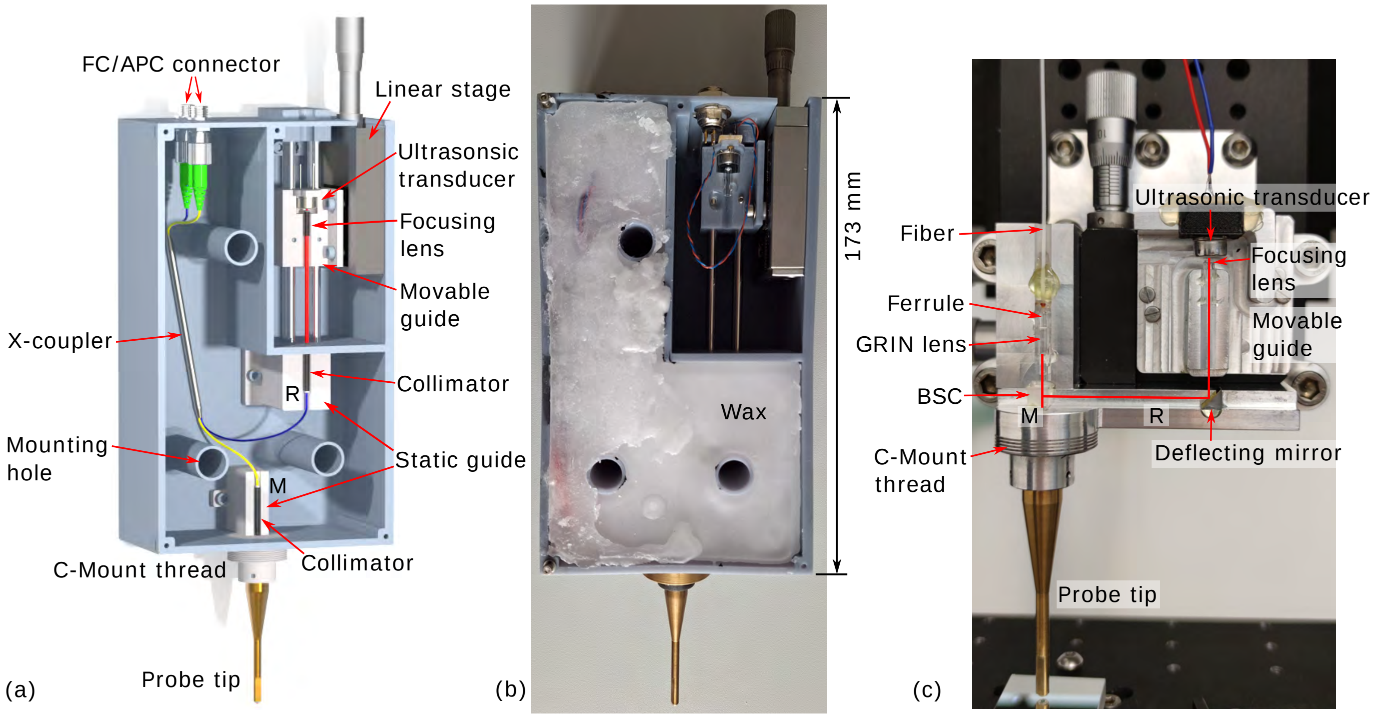

Figure 2. Schematic drawing (**a**) and photograph (**b**) of the FICDS, where measurement (M) and reference (R) arms are coupled by a fiber x-coupler. In (**b**), the fiber-optical components are encapsulated in wax to prevent external vibrations from affecting the fiber-guided laser beams. An alternative free-beam interferometer where the light is split by a beam splitter cube (BSC) into measurement (M) and reference (R) arm is shown in (**c**). The red lines represent the free-beam paths.

2.2. Signal Processing

The resulting two-beam interference signal I_{int} is given by

$$I_{\mathrm{int}} = I_{\mathrm{m}} + I_{\mathrm{ref}} + 2V\sqrt{I_{\mathrm{m}} I_{\mathrm{ref}}} \cos\left(\frac{4\pi}{\lambda}(z_{\mathrm{m}} - z_{\mathrm{ref}})\right), \tag{1}$$

where I_{m} and I_{ref} represent the intensities of the measurement and the reference arm. z_{m} and z_{ref} are the corresponding path-length deviations of the measurement and the reference arm with respect to balanced interferometer arms. The laser wavelength is considered by λ. Due to the fact that a laser of high temporal coherence length is used, the visibility V can be taken as unity for such a profilometer. A more comprehensive formulation considering the focusing by the lenses is given in [16]. In order to enable height discrimination based on the phase of the interference signal, the OPD is modulated sinusoidally by an ultrasonic transducer with a polished surface acting as reference mirror. This is considered in Equation (1) by

$$z_{\mathrm{ref}} = z_{\mathrm{a}} \cos\left(2\pi f_{\mathrm{a}} t - \phi_{\mathrm{a}}\right) + z_{\mathrm{a0}}. \tag{2}$$

z_{a} represents the amplitude of the axial mirror displacement, ϕ_{a} an arbitrary phase shift, z_{a0} an offset, t the time, and f_{a} the frequency of the oscillating reference mirror. Both the axial deflection of the reference mirror (red) and the modulated interference signal (blue) are depicted in Figure 3. The oscillation frequency f_{a} corresponds to 38 kHz and the amplitude z_{a} is approx. 1.95 µm. Further, a laser that emits light at a wavelength of 1550 nm is used. Around the inflection points of the sinusoidal mirror oscillation, a nearly linear deflection is assumed. Setting $z_{\mathrm{a0}} = 0$ and replacing the cosine in Equation (2) by a sine function due to $\phi_{\mathrm{a}} = 90\,^{\circ}$ for simplification, the argument ϕ of the cosine in Equation (1) can be approximated by a Taylor series:

$$\phi = \frac{4\pi}{\lambda}\left[z_{\mathrm{a}} 2\pi f_{\mathrm{a}} t_{\mathrm{e}} - z_{\mathrm{a}} \frac{(2\pi f_{\mathrm{a}})^3}{6} t_{\mathrm{e}}^3 + z_{\mathrm{a}} \frac{(2\pi f_{\mathrm{a}})^5}{120} t_{\mathrm{e}}^5 - z_{\mathrm{m}}\right] \tag{3}$$

in the temporal space of $t_{\mathrm{e}} = -p/(4f_{\mathrm{a}}), \ \ldots \ , p/(4f_{\mathrm{a}})$ where $p = 0, \ \ldots \ , 1$ limits the considered signal range with respect to $\pm 1/(4f_{\mathrm{a}})$. For $p = 0.5$, the expression in Equation (2) exhibits a maximum deviation of approximately ±0.005% from the original sinusoidal function. This leads to the frequency

$$f = \frac{1}{2\pi}\frac{\mathrm{d}}{\mathrm{d}t_{\mathrm{e}}}\phi = \frac{2}{\lambda}\left[z_{\mathrm{a}} 2\pi f_{\mathrm{a}} - z_{\mathrm{a}} \frac{(2\pi f_{\mathrm{a}})^3}{2} t_{\mathrm{e}}^2 + z_{\mathrm{a}} \frac{(2\pi f_{\mathrm{a}})^5}{24} t_{\mathrm{e}}^4\right] \tag{4}$$

carrying the phase shift related to z_{m}. Thus, along with a frequency peak at $4\pi z_{\mathrm{a}} f_{\mathrm{a}}/\lambda$, additional components at slightly lower frequencies are present in the spectrum, leading to a frequency centroid of

$$f_{\mathrm{e}} = \frac{\sum \tilde{I}_{\mathrm{int}}(f) f}{\sum \tilde{I}_{\mathrm{int}}(f)} \tag{5}$$

used to analyze the Fourier transformed interference signal $\tilde{I}_{\mathrm{int}}(f)$. While the turning points of the reference mirror oscillation are not taken into account, the signal sections, where the phase is proportional to t_{e}, are used for phase analysis and exemplarily highlighted in Figure 3 as evaluation windows by a green area for the rising and an orange area for the falling flank of the mirror oscillation. The constant frequency f_{e} enables the determination of a height value by calculating the cosine argument ϕ in Equation (1), using a lock-in phase analysis algorithm for each evaluation window, as described in [16,17].

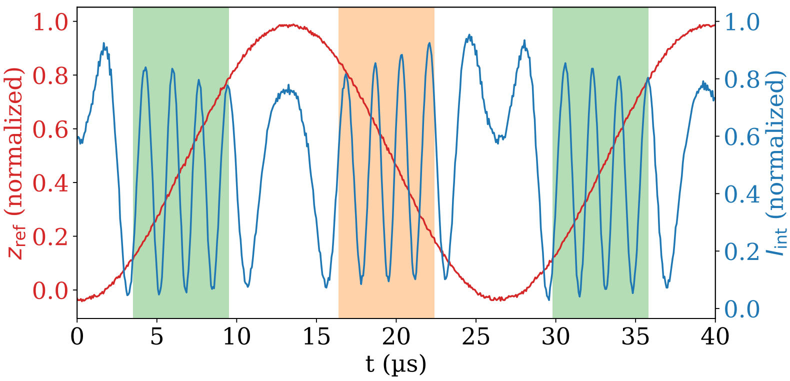

Figure 3. Captured interference signal I_{int} (blue), depending on the axial deflection z_{ref} (red) of the reference mirror, oscillating with a frequency of 38 kHz. The green areas mark the evaluation window for a rising and the orange for a falling flank of the reference mirror oscillation.

The difference $\Delta\phi$ of phase values obtained from two consecutive evaluation windows of equal actor flanks results in the height difference

$$\Delta z_{\mathrm{m}} = \frac{\lambda}{4\pi}\Delta\phi \tag{6}$$

of two consecutive height values z_{m}. Hence, a maximum rate of height values of twice the oscillation frequency f_{a} results when the interference signals obtained at both flanks are considered. In the case of using the interference signal at only one flank of the oscillating mirror, the height value rate equals f_{a}. Note that the amplitude of the oscillating reference mirror corresponds to at least one wavelength of the laser light. The resulting fringe frequency f_{e} is calibrated automatically by a reference measurement prior to each measuring process. In this calibration procedure, the frequency with regard to Equation (5) is determined and used throughout the lock-in signal processing algorithm. Therefore, constant oscillation amplitude z_{a} and frequency f_{a} are assumed. Disturbing effects affecting the measured height such as wavelength drift, interference with spurious reflections, amplitude variation of the oscillating reference mirror, and non-linearity of the used detector are investigated in several studies [15,16,28,29] but are not part of this contribution.

3. Results

This section deals with measurement results related to different specimens. First, profiles obtained from a chirp standard are presented for two different lateral scan velocities. Then, results obtained from a sinusoidal standard are shown and, finally, the standard deviation of repeated measurements as well as the improvement in terms of the number of averaged height values are discussed. For these investigations, the sensor is integrated into a multisensor measuring system [30], where it can be vertically positioned by a linear stage. The object under investigation is placed on two horizontally arranged air-bearing stages to perform the lateral scan. Further, external vibrations are compensated by the multisensor setup.

3.1. Chirp Standard

Due to a sinusoidal surface texture with increasing spatial frequency, a chirp standard is suitable to investigate the transfer behavior of a profilometer and is accordingly often used for sensor characterization. Here, a chirp standard manufactured by the PTB (Physikalisch-technische Bundesanstalt, Germany) [31], including a coarse and fine texture, is used. The coarse texture is characterized by nominal spatial period lengths in the range of 10 µm to 91 µm, whereas the fine texture shows a nominal period length between 3.8 µm and 12 µm, as documented by reference measurements using an atomic force microscope (AFM) [30]. Both textures exhibit a nominal peak-to-valley (pv) amplitude of 400 nm.

The results of the coarse chirp measured by the FICDS are shown in Figure 4 for a lateral scan velocity v_{s} of (a) 20 mm/s and (b) 100 mm/s. For both scan speeds, the chirp profile is well-resolved. However, the profile measured with 100 mm/s is superimposed by additional oscillations. These oscillations originate from the transient response of the scan axis during acceleration and can be eliminated by appropriate high-pass filtering. Comparing the results in Figure 4, a difference in the measured period lengths can be seen at a lateral position of 1 mm. This difference can be attributed to a non-constant scan velocity of the 100 mm/s scan as a consequence of the deceleration process.

Similar results can be taken from the profiles obtained at the fine chirp texture, which are depicted in Figure 5. As in case of the coarse chirp, the profile of the fine chirp measured at 100 mm/s is superimposed by additional oscillations caused by the acceleration of the scan axis. In contrast, such an influence cannot be observed in the profile obtained for 20 mm/s. However, vibrations caused by the air stream of the scan axis's air bearing affect the profiles obtained for both scan speeds in various strengths, as discussed in more detail in [16]. While the chirp texture can be resolved laterally with the FICDS at a scan velocity of 20 mm/s, the texture in the center of the fine chirp is undersampled at the highest spatial frequencies due to the velocity-dependent sampling interval

$$\Delta x = \frac{v_\mathrm{s}}{f_\mathrm{a}}, \tag{7}$$

which is proportional to the scan velocity.

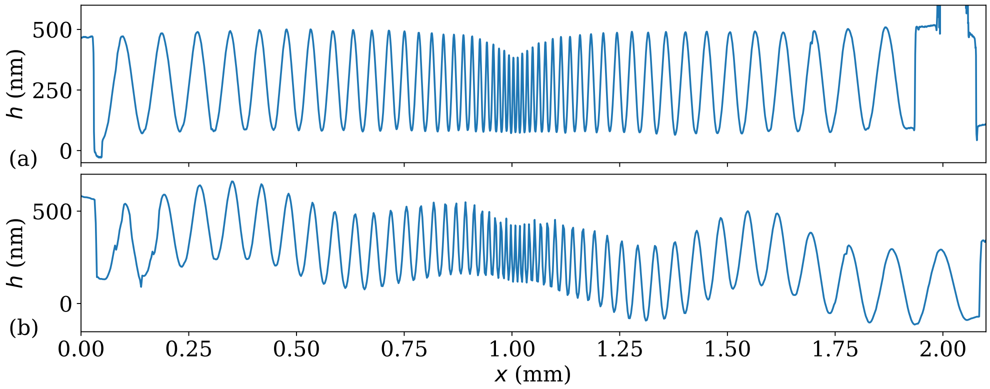

Figure 4. Coarse chirp profiles measured by the FICDS with a lateral scan velocity of (**a**) 20 mm/s and (**b**) 100 mm/s.

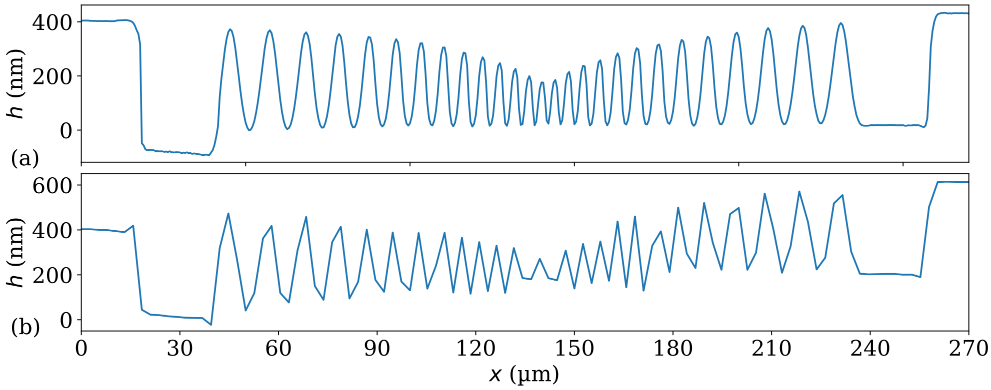

Figure 5. Fine chirp texture measured by the FICDS with a lateral scan velocity of (**a**) 20 mm/s and (**b**) 100 mm/s.

In the case where v_s = 20 mm/s, a sampling interval of 0.53 µm results, while the interval increases to 2.6 µm at 100 mm/s. Nevertheless, the lateral sampling interval can be reduced by a factor of two when considering the height values determined by the second evaluation window, as shown in [15]. As well as the sampling interval, the focused laser spot width must be taken into account to describe the low-pass filtering of the measured surface texture, as discussed in [30].

Due to the increasing spatial frequency towards the center of the chirp, this texture is suitable for determining the lateral resolution of a sensor. For this purpose, the strength of low-pass filtering can be taken into account. Although the same degree of constriction is to be expected on both the top and the bottom of a profile, the profiles depicted in Figure 5 show a one-sided constriction only. This is a result of sharp-combed peaks in the center of the chirp, as determined by a comparison measurement using an AFM [30]. Considering a profile measured by an AFM as reference texture, the NA of the FICDS can be determined as presented in [30]. Therefore, the AFM profile is low-pass filtered by a moving average filter, where the window size is changed after each filtering process until the filtered AFM profile fits best to the profile measured by the FICDS, visualized in Figure 6. As a result of this kind of characterization, an NA of approximately 0.38 is determined for the FICDS, which is improved compared to the miniaturized sensor investigated in [17]. This is due to the fact that, in the FICDS, a different GRIN lens is used, which results in a full illumination of the focusing lens and, thus, increases the NA. Note that the profiles measured by FICDS and AFM are not obtained from the identical position of the chirp standard, and the orientations of the lateral scans may also differ slightly, resulting in minor profile deviations. However, the constriction of each profile at the highest frequency of the chirp is in good agreement.

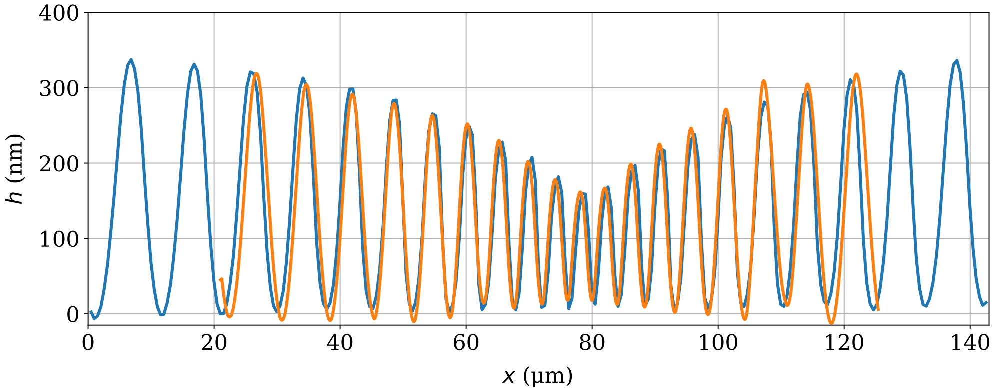

Figure 6. Comparison between profiles measured by FICDS (blue) with a scan velocity of 20 mm/s and AFM (orange). The profile obtained by the AFM is filtered by a moving average filter with a window width corresponding to the parameters of FICDS.

3.2. Sinusoidal Standard

An advantage of point-wise measuring profilometers against microscopic full-field measurement is the ability to measure laterally extended surface profiles in a short time, without the necessity of error-prone stitching. In order to investigate this sensor capability, the sinusoidal standard 531 from Rubert & Co. Ltd. (Cheadle in UK) [32] with a pv-amplitude of 1 µm and a period length of 100 µm is used. The sinusoidal structure extends over a lateral distance of approx. 27 mm. Note that the surface is flat before and after the sinusoidal texture. While the maximum lateral scan velocity v_s is usually limited to 1 mm/s for tactile stylus instruments, much higher velocities can be achieved by the FICDS, as shown in Figure 7. The sinusoidal texture is measured at several scan velocities from 20 mm/s up to 160 mm/s. As can be taken from the profiles depicted in Figure 7a, the sinusoidal texture is superimposed by a nearly parabolic shape. This shape is confirmed by a reference measurement performed by a tactile stylus instrument presented in [17]. In addition to the shape, the measured profiles are superimposed by additional oscillations. These oscillations are again a result of vibrations caused by the acceleration of the scan axis and increase with rising scan velocity. In the case of the profile measured with a scan velocity of 160 mm/s, the sinusoidal texture extends over a longer lateral range compared to the profiles obtained at other scan velocities. This deviation results from the fact that a constant velocity is assumed to determine the x-position.

However, the axis acceleration is not high enough to reach the scan velocity of 160 mm/s at the beginning of the sinusoidal texture. The same can be observed at the end of the profile caused by the deceleration of the axis. One possibility to reduce these deviations is to track the lateral position of the scan axis using its quadrature encoder, as performed for lower scan velocities. For this purpose, the encoder must be adjusted to such high scan velocities. Nonetheless, the sinusoidal texture is determined for all scan velocities, leading to a pv-amplitude of approximately 1 µm and 100 µm period length, as shown in Figure 7b. Small deviations from the ideal sine-shaped texture, e.g., due to impurities, are filtered more strongly with increasing scan velocity, as shown in Figure 8. The profile recorded at 20 mm/s exhibits systematic deviations at the same position on the flanks of the sinusoidal texture, the cause of which needs to be investigated in future work.

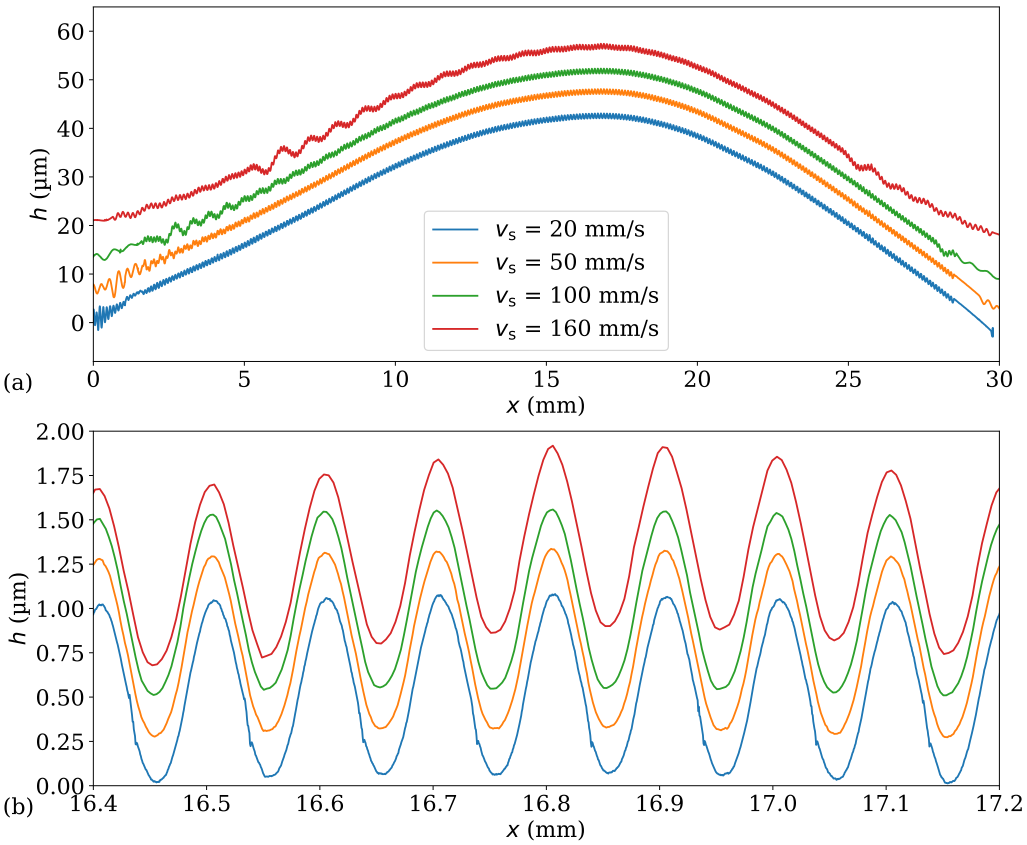

Figure 7. Measurement results obtained from the sinusoidal standard Rubert 531 measured by the FICDS at different lateral scan velocities v_s. The profiles of the whole laterally extended sinusoidal texture are depicted in (**a**) and sections of these profiles are plotted in (**b**). Note that different vertical offsets are added to the profiles for better visualization.

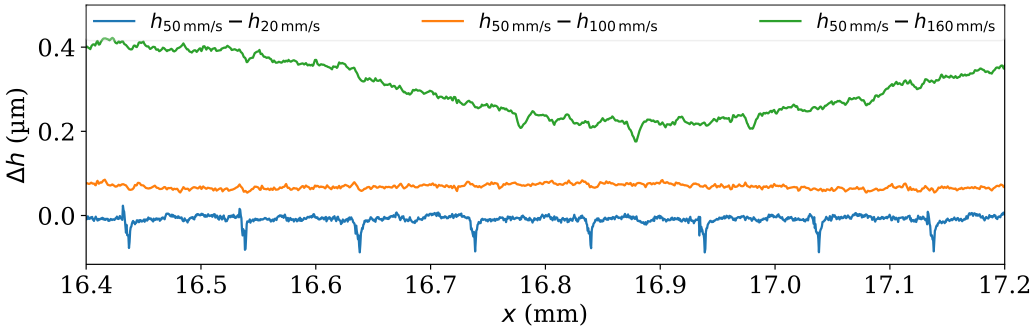

Figure 8. Differences Δh between the profiles depicted in Figure 7. The differences are separated vertically by an overlay with different offsets for better visualization.

In addition, the averaged pv-amplitudes $\overline{h}_\mathrm{pv}$ are listed in Table 1. Note that these values are calculated using eight different pv-amplitudes obtained from the sinusoidal texture depicted in Figure 7. The determined averaged pv-amplitudes agree well with the nominal value of 1 µm; the deviations $\overline{\epsilon}$ are less than 0.9%. These deviations might be the result of vertical vibrations caused by the scan axis, which vary for each scan velocity. Furthermore, differently filtered impurities concerning the lateral scan velocity v_s may contribute to the determined pv-amplitudes. The individual pv-amplitudes used to calculate $\overline{h}_\mathrm{pv}$ vary, as they are represented by the standard deviation σ_pv of the investigated eight pv-amplitudes. While the values obtained for scan velocities up to 100 mm/s are below 10 nm, the standard deviation determined for 160 mm/s is approximately 37 nm. This can be attributed to the additional oscillations that extend over the entire measured profile and, thus, can be reduced by increasing the lateral scan range by an offset. The axial repeatability of the FICDS is discussed in the following section.

Table 1. Averaged pv-amplitudes $\overline{h}_{\mathrm{pv}}$ obtained from eight measurements of the sinusoidal texture depicted in Figure 7b for various scan velocities v_{s}. The variations of the determined pv-amplitudes are expressed by the standard deviation σ_{pv}. $\overline{\epsilon}$ represents the deviation of $\overline{h}_{\mathrm{pv}}$ from the nominal pv-amplitude of 1 µm.

v_{s} (mm/s)	$\overline{h}_{\mathrm{pv}}$ (nm)	$\overline{\epsilon}$ (nm)	σ_{pv} (nm)
20	1000.9	0.9	8.34
50	996.6	3.4	7.12
100	991.1	8.9	9.10
160	999.3	0.7	37.44

3.3. Repeatability

The measurement results discussed so far deal with the sensor’s ability to resolve small geometry features laterally and to measure laterally extended textures at high scan velocities. In this section, the axial repeatability of the FICDS is investigated. For this purpose, 456,000 height measurements are repeated at the identical point of an aluminum mirror. This corresponds to a measurement time of 12 s at a height acquisition rate of 38 kHz. The measured height values are plotted in Figure 9a and a short section of 50 ms is depicted in Figure 9b. Note that only an equalizing line is removed from the tuple of measured height values to remove a drift caused by, e.g., temperature-based material extensions or drifts by the axial positioning axis. No additional filter is applied to the measured height values used in the following. Further, the air bearing of the lateral scan axes is disabled to avoid vibrations caused by the air stream of the air bearing, which can affect the measured height values as discussed previously with enabled air-bearing. Since the FICDS is integrated into a multisensor measuring system, external vibrations are blocked by active vibration compensation combined with the mass inertia of a granite construction. However, the laboratory is located on the fourth floor and a main street with a tram station is in front of the building, which mean that the influence of external vibrations cannot be completely ruled out. Nevertheless, it is expected that the deviations of the repeated measurements are a result of the sensor’s noise and, thus, primarily the repeatability of the sensor is investigated.

Figure 9c shows the frequency spectrum of the measured height values depicted in Figure 9a. Due to the height acquisition rate of 38 kHz, oscillations with a maximum frequency of 19 kHz can be detected by the FICDS. Most spectral amplitudes $\hat{h}$ depicted in Figure 9c are very low. Higher amplitudes occur, especially at lower frequencies, as shown in Figure 9d. Here, the highest peak appears with an amplitude of 140 pm at a frequency of approximately 0.24 Hz. The repeatability of the sensor results from the standard deviation σ of measured height values. While the high acquisition rate is used to measure surface textures with high scan velocities in the previous sections, the high data rate can be alternatively used to improve the repeatability by averaging height values h before calculating the standard deviation

$$\sigma \approx \sqrt{\frac{n_{\mathrm{w}}}{n} \sum_{j=0}^{n/n_{\mathrm{w}}-1} (\overline{h}_j - \overline{h})^2} \tag{8}$$

with a tuple of n_{w} averaged height values

$$\overline{h}_j = \frac{1}{n_{\mathrm{w}}} \sum_{i=jn_{\mathrm{w}}}^{n_{\mathrm{w}}-1+jn_{\mathrm{w}}} h_i \tag{9}$$

and the average of all (n) considered height values

$$\bar{h} = \frac{n_\mathrm{w}}{n} \sum_{j=0}^{n/n_\mathrm{w}-1} \frac{1}{n_\mathrm{w}} \sum_{i=jn_\mathrm{w}}^{n_\mathrm{w}-1+jn_\mathrm{w}} h_i = \frac{1}{n} \sum_{i=0}^{n-1} h_i. \tag{10}$$

Here, $i \in \mathbb{N}_0$ represents the index with respect to every single height value and $j \in \mathbb{N}_0$ is the index regarding the averaged height values. To illustrate the improvement, the calculation according to Equation (8) is applied to the measured height values for various values of n_w and the result is depicted in Figure 9e. Although a decreased standard deviation occurs with increasing n_w, the resulting height value rate f_h also decreases. This is exemplarily compared in numbers for some representative n_w in Table 2. Note that f_h can be increased by use of an ultrasonic transducer that oscillates at a higher frequency, e.g., at 58 kHz, as is reported in [30]. Without averaging the measured height values (i.e., n_w = 1), the standard deviation of FICDS repeatability measurements is 625.9 pm. This value is slightly below the standard deviation of 772.6 pm obtained for the sensor depicted in Figure 2c. However, the theoretical reduction of the standard deviation of uncorrelated random numbers by $1/\sqrt{n_\mathrm{w}}$ due to averaging (Bienaymé equation) is not achieved. This may be caused by correlated sequential noise values.

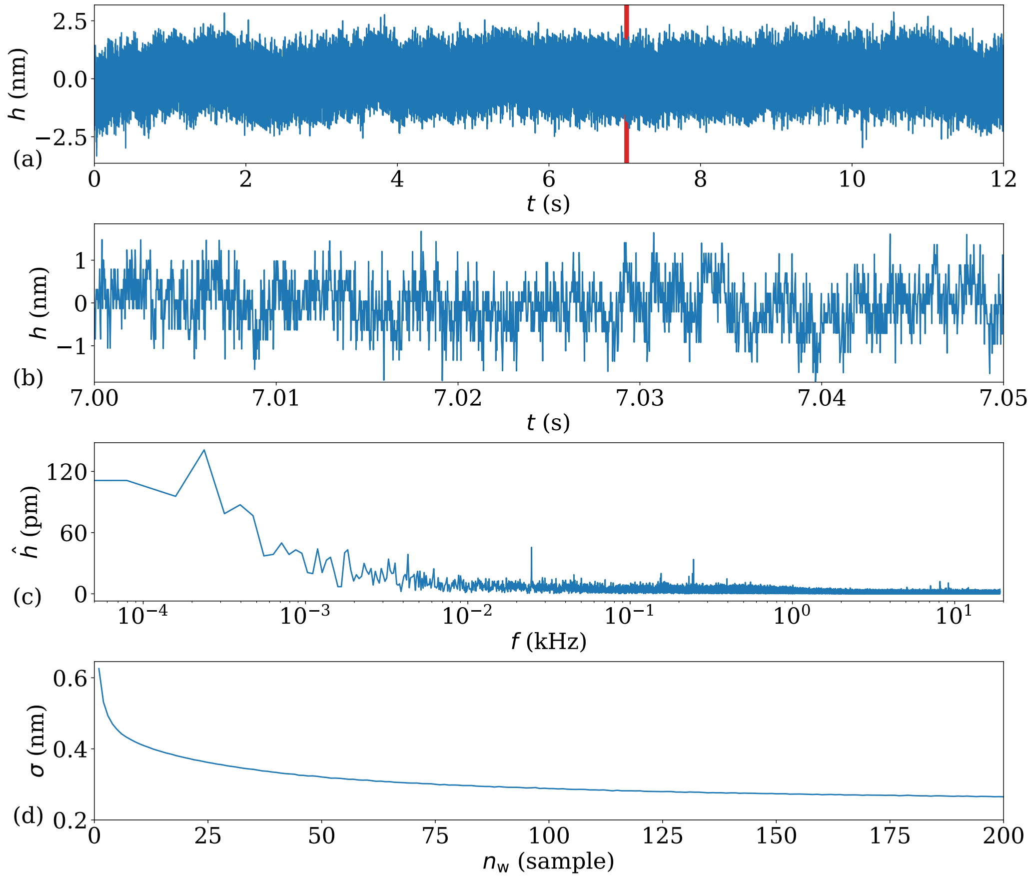

Figure 9. (**a**) A total of 456,000 height values h obtained by the FICDS at the same location of an aluminum mirror, (**b**) section of 1900 height values extracted from (**a**) in the red marked section, (**c**) Fourier domain representation of the data set shown in (**a**) containing frequency-dependent amplitudes $\hat{h}$, and (**d**) the standard deviation σ of the averaged height values of number n_w.

Table 2. Standard deviations σ and height value rate f_h with respect to the number of averaged height values n_w.

n_w **(Sample)**	σ **(pm)**	f_h **(Hz)**
1	625.9	38,000
2	531.9	19,000
5	454.3	7600
10	413.6	3800
100	288.2	380
200	265.0	190

Note that the measurements to determine the repeatability are performed on an aluminum mirror. If the specimen consists of a different medium with lower reflectivity than an aluminum mirror, the contrast of the detected interference signal decreases and, thus, the signal-to-noise ratio results in a higher repeatability value. However, the signal contrast is not limited by the dynamic range of a camera as a consequence of an intensity offset, which occurs in interferometric sensors (e.g., coherence scanning interferometer), where a camera is used for signal detection. A comparison between the repeatability obtained from an aluminum mirror and a glass plate as specimens is shown in [16] for the same measurement principle. Here, the standard deviation increases from 1 nm to approx. 1.8 nm. A similar principle applies to rough surfaces. The ability to measure rough surfaces with such a sensor principle is presented in [16,17].

4. Conclusions

In this study, we present a high-speed laser interferometer where the measurement and reference arm are separated by an optical fiber coupler instead of a beam-splitter cube. We solve the well-known problem that fiber optic interferometers may be disturbed by any kind of movement or vibration by embedding both fiber-optic interferometer arms into wax, thus achieving an outstanding performance in distance measurement. This is proven by several measurements on specimens of different textures. While the whole sensor setup is larger in its geometrical dimensions compared to previous more compact designs, the thin probe tip enables the measurement of surface textures at hard-to-access locations. In addition, due to the fact that the sensor works in a wavelength regime of ≈1550 nm, as is typically used for fiber-optic communication solutions, its costs are quite low. In addition to the ability to measure surface profiles with high lateral resolution even at high scan velocities, a repeatability of approximately 625 pm has been demonstrated. While the measurement uncertainty is determined based on repeated measurements on an aluminum mirror, the measurement uncertainty of height textures has not been fully investigated in this contribution. However, the sensor's NA of 0.38 and, thus, the ability to calculate its lateral resolution according to the Gaussian ray principle are determined by comparing the results obtained from a chirp standard with a laterally filtered reference profile measured by an AFM. Further, the pv-amplitudes of the measured sinusoidal profiles exhibit averaged deviations of less than 0.9% with regard to the nominal pv-amplitude of 1 µm. In this context, results for lateral scan velocities up to 160 mm/s are presented. Note that 160 mm/s is not the limit of the sensor, but originates from the lateral scan axis. In addition, it is shown that the repeatability can be further improved by averaging while still providing data rates that are acceptable for many applications. The position of the scan axis is tracked by the scan axis's quadrature encoder synchronously to the acquired height values. In the case of fast lateral scan velocities ($\geq$50 mm/s), a linear axis motion of constant velocity is assumed to calculate the position of each acquired height value virtually. In future work, the encoder signal and also the signal processing algorithm could be modified to cope with higher scanning velocities.

Author Contributions: Conceptualization, S.H. and Y.Z.; methodology, S.H.; software, S.H.; validation, S.H. and Y.Z.; formal analysis, S.H.; investigation, S.H., Y.Z., T.P. and F.R.; resources, P.L.; data curation, S.H.; writing—original draft preparation, S.H.; writing—review and editing, Y.Z., T.P., F.R. and P.L.; visualization, S.H. and Y.Z.; supervision, P.L.; project administration, S.H. and P.L.; funding acquisition, P.L. All authors have read and agreed to the published version of the manuscript.

Funding: This research was funded by Deutsche Forschungsgemeinschaft (DFG, Germany), grant number LE 992/17-1.

Institutional Review Board Statement: Not applicable.

Informed Consent Statement: Not applicable.

Data Availability Statement: Data available in a publicly accessible repository.

Conflicts of Interest: The authors declare no conflict of interest.

Abbreviations

The following abbreviations are used in this manuscript:

A	Actuator
AD	Actor driver
ADC	Analog-to-digital converter
AFM	Atomic force microscopy
APC	Angled physical contact
BSC	Beam-splitter cube
DAC	Digital-to-analog converter
FC	Ferrule connector
FICDS	Fiber-coupled interferometric confocal distance sensor
FPGA	Field programmable gate array
HMSC	High-speed mezzanine card
LD	Laser driver
M	Measurement arm
NA	Numerical aperture
OPD	Optical path-length difference
PC	Personal computer
PD	Photodiode driver
PTB	Physikalisch-technische Bundesanstalt, Germany
PV	Peak-to-valley
R	Reference arm
SPU	Signal processing unit
X	Fiber-based x-coupler

References

1. Song, J.F.; Vorburger, T.V. Stylus profiling at high resolution and low force. *Appl. Opt.* **1991**, *30*, 42–50. [CrossRef] [PubMed]
2. Whitehouse, D.J. *Surface and Their Measurement*, 1st ed.; Kogan Page Science: London, UK, 2002.
3. Lee, D.H.; Cho, N.G. Assessment of surface profile data acquired by a stylus profilometer. *Meas. Sci. Technol.* **2012**, *23*, 105601. [CrossRef]
4. *DIN EN ISO 3274*; Geometrical Product Specification (GPS)—Surface Texture: Profile Method—Nominal Characteristics of Contact (Stylus) Instruments. International Organization for Standardization: Geneva, Switzerland, 1996.
5. Molesini, G.; Pedrini, G.; Poggi, P.; Quercioli, F. Focus-wavelength encoded optical profilometer. *Opt. Commun.* **1984**, *49*, 229–233. [CrossRef]
6. Ruprecht, A.; Wiesendanger, T.; Tiziani, H. Chromatic confocal microscopy with a finite pinhole size. *Opt. Lett.* **2004**, *29*, 2130–2132. [CrossRef] [PubMed]
7. Wertjanz, D.; Kern, T.; Csencsics, E.; Stadler, G.; Schitter, G. Compact scanning confocal chromatic sensor enabling precision 3-D measurements. *Appl. Opt.* **2021**, *60*, 7511–7517. [CrossRef] [PubMed]
8. Mastylo, R.; Dontsov, D.; Manske, E.; Jager, G. A focus sensor for an application in a nanopositioning and nanomeasuring machine. *SPIE Proc.* **2005**, *5856*, 238–244.
9. Rao, Y.J.; Jackson, D.A. Recent progress in fibre optic low-coherence interferometry. *Meas. Sci. Technol.* **1996**, *7*, 981. [CrossRef]
10. Depiereux, F.; Hamm, W.; Schmitt, R.; Mallmann, G.F. Fiber-Optical Interferometer for Distance Measurements: Investigation of Linearity Linearitätsuntersuchungen eines faseroptischen Distanzmesssystems. *Tm-Tech. Mess.* **2009**, *76*, 374–377. [CrossRef]

11. Beutler, A. Flexible, non-contact and high-precision measurements of optical components. *Surf. Topogr. Metrol. Prop.* **2016**, *4*, 024011. [CrossRef]
12. Schulz, M.; Lehmann, P. Measurement of distance changes using a fibre-coupled common-path interferometer with mechanical path length modulation. *Meas. Sci. Technol.* **2013**, *24*, 065202. [CrossRef]
13. Sharma, S.; Eiswirt, P.; Petter, J. Electro optic sensor for high precision absolute distance measurement using multiwavelength interferometry. *Opt. Express* **2018**, *26*, 3443–3451. [CrossRef] [PubMed]
14. Sharma, S.; Eiswirt, P.; Petter, J. Multi-wavelength Interferometric Distance Sensors. In *Advances in Optics: Reviews*; IFSA Publishing, s.l.: Barcelona, Spain, 2019; Volume 4, Chapter 10, pp. 239–264.
15. Hagemeier, S.; Tereschenko, S.; Lehmann, P. High-speed laser interferometric distance sensor with reference mirror oscillating at ultrasonic frequencies. *Tm-Tech. Mess.* **2019**, *86*, 164–174. [CrossRef]
16. Hagemeier, S. Comparison and Investigation of Various Topography Sensors Using a Multisensor Measuring System. Ph.D. Thesis, University of Kassel, Kassel, Germany, 2022.
17. Hagemeier, S.; Bittner, K.; Depiereux, F.; Lehmann, P. Miniaturized interferometric confocal distance sensor for surface profiling with data rates at ultrasonic frequencies. *Meas. Sci. Technol.* **2023**, *34*, 045104. [CrossRef]
18. Riebeling, J.; Ehret, G.; Lehmann, P. Optical form measurement system using a line-scan interferometer and distance measuring interferometers for run-out compensation of the rotational object stage. *SPIE Proc.* **2019**, *11056*, 607–613.
19. Serbes, H.; Gollor, P.; Hagemeier, S.; Lehmann, P. Mirau-based CSI with oscillating reference mirror for vibration compensation in in-process applications. *Appl. Sci.* **2021**, *11*, 9642. [CrossRef]
20. TerasIC Inc. *Overview of AD/DA Data Conversion Card* . Available online: https://www.terasic.com.tw/cgi-bin/page/archive.pl?Language=English&CategoryNo=73&No=360&PartNo=1#contents (accessed on 14 May 2024).
21. PD-LD Inc. *PL13/15 DFB Series Laser Diode Modules*. 2016. Available online: https://www.lasercomponents.com/fileadmin/user_upload/home/Datasheets/pd_ld/pl1315dfb.pdf (accessed on 11 July 2024).
22. TerasIC Inc. *Overview of SoCKit*. Available online: https://www.terasic.com.tw/cgi-bin/page/archive.pl?Language=English&CategoryNo=167&No=816&PartNo=1#contents (accessed on 14 May 2024).
23. Grintech. *GRIN Rod Lenses—Numerical Aperture 0.2*. 2019. Available online: https://www.grintech.de/fileadmin/Kunden/Datenblaetter/rev.12-2022/GRIN_Rod_Lenses_Numerical_Aperture_02.pdf (accessed on 11 July 2024).
24. Shin, H.J.; Pierce, M.C.; Lee, D.; Ra, H.; Solgaard, O.; Richards-Kortum, R. Fiber-optic confocal microscope using a MEMS scanner and miniature objective lens. *Opt. Express* **2007**, *15*, 9113–9122. [CrossRef]
25. Meier, M.; Weichert, C.; Kawohl, J.; Flügge, J.; Manske, E. Comparison of full fiber coupled interferometer systems under vacuum conditions. *Tm-Tech. Mess.* **2024**, *91*, 281–288. [CrossRef]
26. Anycubic Ltd. *Overview of Anycubic Photon Mono M5s*. Available online: https://store.anycubic.com/products/photon-mono-m5s (accessed on 14 May 2024).
27. Pfeifer, T.; Schmitt, R.; Konig, N.; Mallmann, G.F. Interferometric measurement of injection nozzles using ultra-small fiber-optical probes. *Chin. Opt. Lett.* **2011**, *9*, 071202. [CrossRef]
28. de Groot, P. Design of error-compensating algorithms for sinusoidal phase shifting interferometry. *Appl. Opt.* **2009**, *48*, 6788–6796. [CrossRef]
29. Tereschenko, S. Digitale Analyse Periodischer und Transienter Messsignale Anhand von Beispielen aus der Optischen Präzisionsmesstechnik. Ph.D. Thesis, University of Kassel, Kassel, Germany, 2018.
30. Hagemeier, S.; Schake, M.; Lehmann, P. Sensor characterization by comparative measurements using a multi-sensor measuring system. *J. Sens. Sens. Syst.* **2019**, *8*, 111–121. [CrossRef]
31. Brand, U.; Doering, L.; Gao, S.; Ahbe, T.; Buetefisch, S.; Li, Z.; Felgner, A.; Meess, R.; Hiller, K.; Peiner, E.; et al. Sensors and calibration standards for precise hardness and topography measurements in micro-and nanotechnology. In Proceedings of the Micro-Nano-Integration, 6. GMM-Workshop, Duisburg, Germany, 5–6 October 2016; pp. 1–5.
32. Rubert & Co., Ltd. *Reference Specimens*. Available online: http://www.rubert.co.uk/reference-specimens/ (accessed on 16 May 2024).